

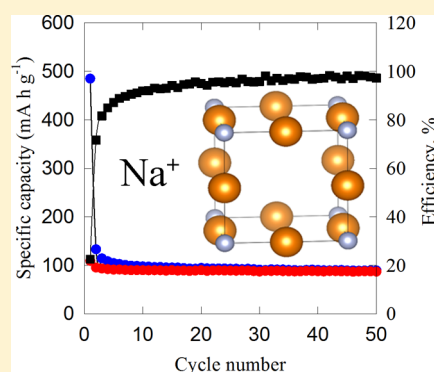
# Evaluation of $\text{Cu}_3\text{N}$ and $\text{CuO}$ as Negative Electrode Materials for Sodium Batteries

Xianji Li, Andrew L. Hector,\* and John R. Owen

Chemistry, University of Southampton, Highfield, Southampton SO17 1BJ, U.K.

## S Supporting Information

**ABSTRACT:** Copper(I) nitride, produced by the ammonolysis of copper(II) pivalate at 250 °C, shows a competitive capacity and stable cycling behavior in sodium cells with a  $\text{NaPF}_6$ /ethyl carbonate/diethyl carbonate electrolyte. Ex situ X-ray diffraction studies suggest that this material acts as a conversion electrode, with  $\text{Cu}_3\text{N}$  reduced to copper metal, but that these reactions occur only at the surfaces of the particles. A higher capacity is observed in lithium cells, again with stable cycling behavior. Hydrolysis results in nanocrystalline  $\text{CuO}$ , which has a higher sodium cell capacity. However, this capacity gradually decays on cycling and, after 30 cycles, is similar to that observed with  $\text{Cu}_3\text{N}$ .



## 1. INTRODUCTION

Sodium-ion batteries have undergone rapid development in recent years due to a recognition that they could provide a competitive alternative to lithium systems that will become increasingly important as economically attractive lithium resources diminish.<sup>1–4</sup> Developing large-scale battery applications in transport and in energy storage linked to intermittent green energy sources such as wind and solar power are further drivers to this process.

Taking inspiration from lithium-ion batteries, a variety of good positive electrode materials for sodium-ion batteries have been developed, including layered transition metal oxides,<sup>5–10</sup> a Prussian blue framework material,<sup>11</sup> and phosphate polyanion structures.<sup>12–14</sup> Graphite is widely used as a safe, efficient negative electrode for lithium-ion batteries, but sodium does not intercalate into it and negative electrode materials remain a significant challenge for sodium-ion batteries.<sup>15</sup> The performance achievable with other carbonaceous materials has recently been improved,<sup>16–19</sup> including significantly a report that hollow carbon nanowires retain 206.3 mA h g<sup>−1</sup> capacity after 400 charge–discharge cycles at 0.2× theoretical capacity per hour (0.2C).<sup>20</sup> Metal alloys can provide high specific capacities;<sup>21–27</sup> e.g., SnSb/C nanocomposites have been shown to retain over 400 mA h g<sup>−1</sup> capacity after 50 cycles at 100 mA g<sup>−1</sup>.<sup>23</sup> These systems suffer from large volume changes during cycling, similar to that of silicon electrodes in lithium-ion batteries, and this may be a disadvantage in construction of working devices. A number of oxides have been investigated,<sup>28–32</sup> including very recently the layered  $\text{Na}_{0.66}[\text{Li}_{0.22}\text{Ti}_{0.78}]\text{O}_2$  system that has only an ~0.77% volume change during sodium insertion/extraction and good stability, although its specific capacity of 118 mA h g<sup>−1</sup> at 0.1C is relatively low.<sup>33</sup> Some organic negative electrode

materials have also been examined, though these suffer from relatively poor stability.<sup>34–36</sup>

We recently reported the first use of a metal nitride negative electrode that could be used in sodium-ion cells.<sup>37</sup>  $\text{Ni}_3\text{N}$  is thought to act as a conversion electrode by reduction to nickel metal, and these reactions at the surface of  $\text{Ni}_3\text{N}$  particles yielded capacities > 100 mA h g<sup>−1</sup> after 30 cycles. Interestingly, ex situ diffraction studies showed that the proportion of the material converted was small, so larger capacities could be available with smaller particle sizes. Copper nitride ( $\text{Cu}_3\text{N}$ , Figure 1) is an intriguing phase for comparison as it adopts an anti- $\text{ReO}_3$  type structure with a vacant site that could be occupied by cations, and which is occupied by further copper atoms in the anti-perovskite  $\text{Cu}_4\text{N}$ .<sup>38–41</sup> Hence, it could operate as an insertion or conversion electrode. In lithium cells, Pereira et al. showed an initial lattice expansion that they attributed to lithium insertion, followed by reduction to copper metal and  $\text{Li}_3\text{N}$ .<sup>42</sup> After an initial loss of capacity, these electrodes provided stable discharge capacities of 140–170 mA h g<sup>−1</sup> at 1.67C, and an unusual gradual increase in capacity when they were oxidized beyond 2 V vs Li, which the authors attributed to oxide formation linked to electrolyte degradation.

Herein, we report the performance of  $\text{Cu}_3\text{N}$  in sodium and lithium half cells.  $\text{CuO}$  electrodes were also obtained when  $\text{Cu}_3\text{N}$  inks were prepared with water, and we also evaluated their electrochemical behavior.  $\text{CuO}$  has previously been examined in sodium cells by Klein et al.,<sup>32</sup> who reported reduction to  $\text{Cu}_2\text{O}$  with a first discharge capacity of ~600 mA h g<sup>−1</sup> at C/10 reducing to 300 mA h g<sup>−1</sup> in the fifth cycle.

**Received:** September 16, 2014

**Revised:** November 24, 2014

**Published:** November 25, 2014

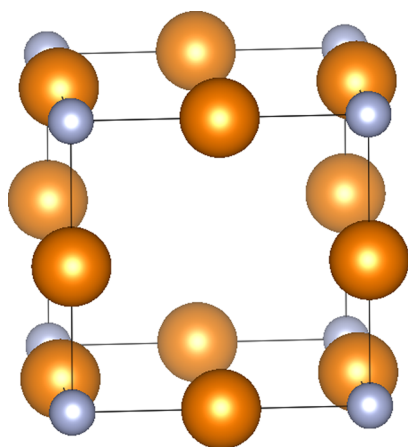


**Figure 1.** Anti- $\text{ReO}_3$  structure of  $\text{Cu}_3\text{N}$  (Cu atoms as large orange spheres, N as small blue spheres) showing the linear  $\text{CuN}_2$  coordination.<sup>38</sup>

## 2. EXPERIMENTAL SECTION

Two methods were used to produce copper nitride samples: (1) Copper fluoride (2 g, Aldrich, 99%) was dried in flowing nitrogen at 140 °C for 6 h and then heated to 300 °C at 2 °C  $\text{min}^{-1}$  under flowing ammonia (BOC anhydrous grade, further dried with 3 Å molecular sieves) and maintained at 300 °C for 8 h. (2) Copper(II) carbonate basic (2 g, Aldrich) was dissolved in 130 mL of deionized water, 5 mL of pivalic acid (Aldrich, 99%) was added, and the solution was stirred for 30 min at 70 °C to release  $\text{CO}_2$ . The dark green copper(II) pivalate precipitate was collected by filtration and washed with deionized water, then ethanol, and then heated under flowing ammonia at 250 °C for 10 h.

Powder X-ray diffraction (XRD) patterns were recorded on a Bruker D2 Phaser using  $\text{Cu-K}\alpha$  radiation in Bragg–Brentano geometry. Rietveld refinements used the GSAS package.<sup>43,44</sup> Ex situ XRD patterns of electrodes before and after electrochemical treatment were collected in grazing incidence geometry (1° incidence angle) with parallel  $\text{Cu-K}\alpha$  X-rays using a Rigaku Smartlab and a sealed, glovebox-loaded sample holder with a thin hemicylindrical Kapton window. Thermogravimetric analyses (TGA) used a Mettler-Toledo TGA/SDTA851e with flowing argon (50 mL  $\text{min}^{-1}$ ). The temperature was raised from 25 to 800 °C at 10 °C  $\text{min}^{-1}$  and was held at maximum temperature for 20 or 60 min. The morphology was examined by transmission electron microscopy (TEM) on a Hitachi H7000 with an accelerating voltage of 75 kV, using samples prepared by ultrasound dispersion into distilled methanol and dropping onto carbon grids. Infrared (IR) spectra were recorded on a PerkinElmer Spectrum 100 FTIR with samples prepared as KBr discs. Surface areas were calculated using the Brunauer–Emmett–Teller (BET) method<sup>45</sup> with nitrogen adsorption data collected using a Gemini 2375 surface area analyzer. Combustion microanalyses (C, H, and N) were outsourced to Medac Ltd., who estimated the error level on these measurements to be around  $\pm 0.30\%$ .

Electrochemical testing used Biologic SP150 and MPG potentiostats. Working electrodes were prepared from a cycloheptanone-based ink of powdered 75% active material, 20% acetylene black (Shawinigan, Chevron Phillips Chemical Co. LP), and 5% PVDF binder (Aldrich). Replacement of the cycloheptanone and PVDF in this process with water and carboxymethyl cellulose in the same quantities resulted in CuO-

based electrodes. The ink was cast onto a 50  $\mu\text{m}$  thick copper foil and air-dried, and then the foil was cut into 10 mm diameter discs. After drying in vacuo, the amount of active material was determined by mass difference. We estimate that the ink compositions are accurate to around 1–2%, and since the electrochemical measurements, e.g., of capacity, are accurate to better than 0.1%, the mass of the active material will be most significant and capacities are reliable to around 1–2%. For ex situ XRD, the same process was applied, but using Ti foil. Two-electrode Swagelok cells were assembled using sodium metal foil (Aldrich, 99.9%) as the counter and pseudo reference electrode. Two sheets of dried Whatman GF/D borosilicate glass fiber were used as the separator, soaked with 6 drops of 1 mol  $\text{dm}^{-3}$   $\text{NaPF}_6$  in ethylene carbonate/diethyl carbonate (1:1) electrolyte. The electrolyte components were purified separately (solvents distilled from BaO and  $\text{NaPF}_6$  dried in vacuo at 120 °C) before combining in the glovebox. A separate evaluation of the likely capacity due to the acetylene black conductivity in the sodium half cells is presented in the Supporting Information, in which we conclude that this is lower than 8 mA h  $\text{g}^{-1}$ . Capacity values discussed in the text are based only on the mass of the  $\text{Cu}_3\text{N}$  active material. Lithium cells were prepared by replacing the sodium with lithium foil (Aldrich, 99.9%) and using a 1 mol  $\text{dm}^{-3}$   $\text{LiPF}_6$  in ethylene carbonate/dimethyl carbonate (1:1) electrolyte (BASF).

## 3. RESULTS AND DISCUSSION

The synthesis of copper nitride is classically achieved by ammonolysis of  $\text{CuF}_2$ ,<sup>38</sup> but can also be accomplished under solvothermal conditions<sup>46</sup> or in solution to make octadecylamine-capped nanoparticles.<sup>47</sup> We compared ammonolysis of  $\text{CuF}_2$  and of a copper(II) pivalate precursor as recently described by Paniconi.<sup>48</sup>

Ammonolysis of  $\text{CuF}_2$  at the literature temperature of 300 °C<sup>43</sup> resulted in crystalline  $\text{Cu}_3\text{N}$  with  $a = 3.81105(5)$  Å and a refined crystallite size of 412(11) nm (Rietveld fit in Figure S1, Supporting Information). Previous reports contain lattice parameters between 3.802 and 3.819 Å.<sup>49</sup> TEM (Figure S2, Supporting Information) showed large, dense particles, suggesting a low accessible surface area. Combustion analysis showed this material to contain 6.6% N (6.8% calculated for  $\text{Cu}_3\text{N}$ ) and no carbon or hydrogen.

Ammonolysis of copper(II) pivalate was carried out at various temperatures with the aim of producing a lower crystallite size and hence higher surface area sample of  $\text{Cu}_3\text{N}$ . At 180 °C, peaks corresponding to  $\text{Cu}_3\text{N}$  were visible in a mixture of phases, at 200 and 250 °C, phase-pure  $\text{Cu}_3\text{N}$  was obtained, and at 300 °C, some decomposition to copper metal was observed (Figure 2). Because of some irreproducibility at 200 °C, samples produced at 250 °C were carried forward for further study. This material was found to have  $a = 3.811495(22)$  Å and a crystallite size of 51.3(1) nm (Figure S3), with TEM showing aggregated particles with average sizes of around 20 nm diameter (Figure S4) (Supporting Information). Combustion analysis showed 6.5% N (6.8% calculated for  $\text{Cu}_3\text{N}$ ) and no detectable carbon or hydrogen.

**3.1.  $\text{Cu}_3\text{N}$  Electrochemistry in Na Half Cells.**  $\text{Cu}_3\text{N}$  electrodes were produced as composites with acetylene black and a PVDF binder by depositing an ink onto copper foil and were cycled against sodium metal using a  $\text{NaPF}_6$  in 1:1 ethylene carbonate/diethyl carbonate electrolyte. Cyclic voltammograms showed multiple reduction steps in the first cycle, some of which will be due to solid electrolyte interface formation, but

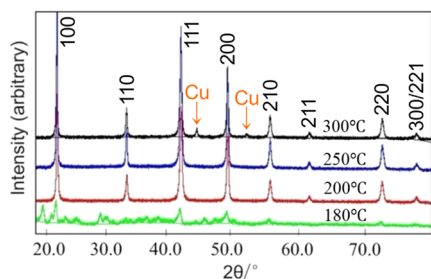


**Figure 2.** Powder XRD pattern of the products of ammonolysis of copper(II) pivalate at various temperatures (10 h heating time).  $\text{Cu}_3\text{N}$  reflections are labeled with Miller indices, and Cu reflections are marked.<sup>49</sup> Phase-pure  $\text{Cu}_3\text{N}$  is obtained at 200 and 250 °C.

quickly settled into a stable loop shape (Figure 3). A pure acetylene black electrode showed an oxidation peak at 0.5 V

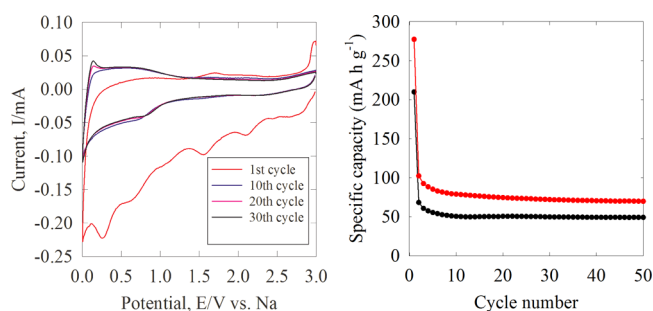


**Figure 3.** Cyclic voltammetry (left) at  $1 \text{ mV s}^{-1}$  of  $\text{Cu}_3\text{N}$  derived from copper pivalate at 1st, 10th, 20th, and 30th cycles, and specific reduction capacity during galvanostatic cycling (right) of pivalate- (red) and  $\text{CuF}_2$ - (black) derived  $\text{Cu}_3\text{N}$  cycled between 3 V and 1 mV at 1C ( $392 \text{ mA h g}^{-1}$ ).

and a broad reduction peak at  $\sim 0.6 \text{ V}$  (Figure S7, Supporting Information). Although it should be noted that pure acetylene black may derive much of its capacity from stacked sheets and, hence, it may yield different signals in a composite electrode, these were not clear in the CV of the  $\text{Cu}_3\text{N}$  composite electrode. However, the reduction peak seen at 0.2 V vs Na in Figure 3 does resemble the peak that appeared at  $\sim 0.5 \text{ V}$  in  $\text{Cu}_3\text{N}/\text{Li}$  half cells,<sup>43</sup> consistent with the  $\sim 0.3 \text{ V}$  difference between the Na and Li scales. The CV was used to set a potential window of 0.001–3 V vs Na for investigation of the capacity of the electrode material.

Galvanostatic cycling initially compared the  $\text{CuF}_2$ - and pivalate-derived materials (Figure 3) at charge/discharge rates of 1C, i.e., full charge or discharge in 1 h based on a theoretical capacity assuming complete reduction of  $\text{Cu}_3\text{N}$  to copper metal and  $\text{Na}_3\text{N}$ . A significant capacity drop is observed between the first and second reduction steps, where reduction would correspond to discharge of a sodium or sodium-ion cell. However, it can be seen that the capacity quickly stabilizes in both materials. The pivalate-derived material has the higher capacity (initial reduction  $277 \text{ mA h g}^{-1}$ , dropping to  $80 \text{ mA h g}^{-1}$  at 10th reduction and  $70 \text{ mA h g}^{-1}$  at 50th), but the more crystalline  $\text{CuF}_2$ -derived  $\text{Cu}_3\text{N}$  still exhibits significant capacity (initial reduction  $210 \text{ mA h g}^{-1}$ , dropping to  $51 \text{ mA h g}^{-1}$  at 10th reduction and  $49 \text{ mA h g}^{-1}$  at 50th). We focused on the pivalate-derived material for variable rate studies, but it should be noted that the capacity is still much lower than expected for complete conversion to Cu and  $\text{Na}_3\text{N}$  ( $392 \text{ mA h g}^{-1}$ ).

Cycling the copper(II) pivalate-derived  $\text{Cu}_3\text{N}$  at various rates under galvanostatic conditions, it was found that, at all rates tried, a large irreversible capacity was observed; i.e., the first reduction ( $277, 343, \text{ or } 485 \text{ mA h g}^{-1}$  at 1C, 0.5C, or 0.1C) was followed by a much smaller amount of charge passed on the first reoxidation ( $102, 117, \text{ or } 133 \text{ mA h g}^{-1}$ ). Figure 4 shows the rapid stabilization of the reduction/oxidation over the first few cycles, with much smaller changes observed in both the

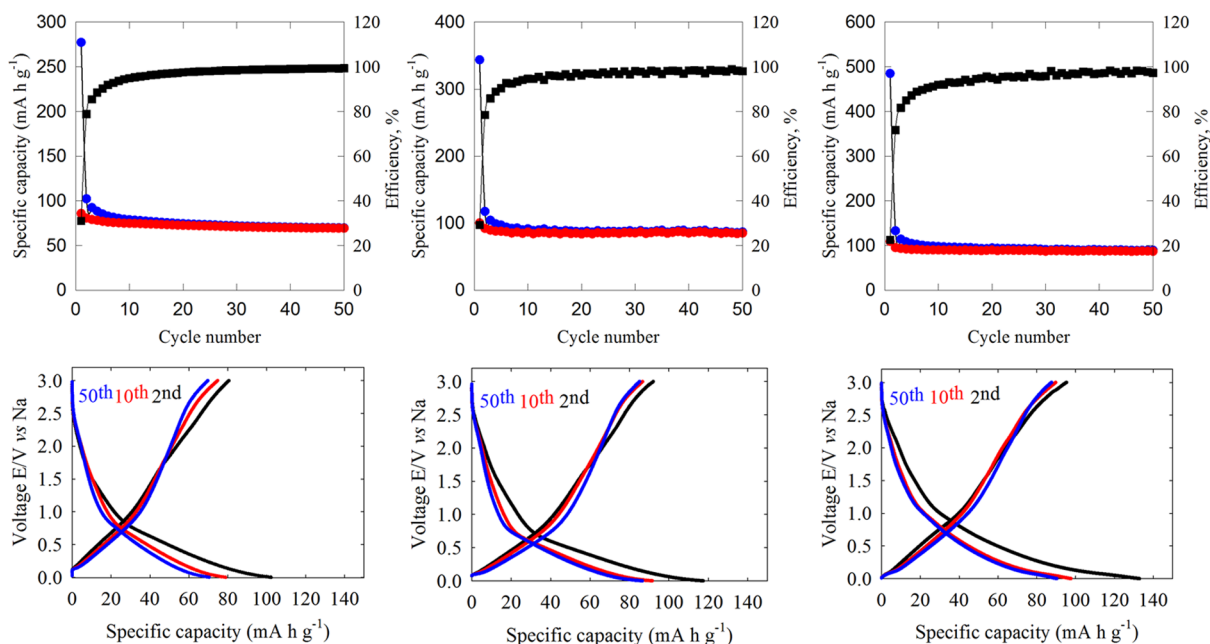


**Figure 4.** Specific capacity versus cycle number (top) and voltage profile in the 2nd, 10th, and 40th cycles (bottom) of  $\text{Cu}_3\text{N}$ -sodium half cells cycled between 1 mV and 3 V at 1C ( $392 \text{ mA h g}^{-1}$ , left), 0.5C ( $196 \text{ mA h g}^{-1}$ , center), and 0.1C ( $39.2 \text{ mA h g}^{-1}$ , right). In the specific capacity vs cycle number plots, blue circles show specific reduction capacity, red circles show specific oxidation capacity, and black squares depict Coulombic efficiency.



reduction (discharge) and the oxidation (charge) processes and efficiency close to 100% from cycle 2 onward. Reduction capacities in the 50th cycles were 70 (1C), 87 (0.5C), or 89 (0.1C)  $\text{mA h g}^{-1}$  using a 3 V cutoff. A high proportion of the reduction capacity was observed in the region below 2 V (261, 311, or 407  $\text{mA h g}^{-1}$  in the 1st cycle, dropping to 66, 82, or 85  $\text{mA h g}^{-1}$  in the 50th), but the oxidation profile slopes more evenly and a smaller proportion of this capacity was in the <2 V region (58, 71, or 69  $\text{mA h g}^{-1}$  becoming 50, 65, or 65  $\text{mA h g}^{-1}$  in the 50th).

Since copper was expected to be one of the products of electrochemical reduction of  $\text{Cu}_3\text{N}$ , it was necessary to change the current collector used for ex situ X-ray diffraction. Titanium foil was found to deliver identical electrochemistry without obscuring the XRD features of interest. Hence, the diffraction pattern of a dried  $\text{Cu}_3\text{N}$  ink before any electrochemical treatment (Figure 5) shows peaks for  $\text{Cu}_3\text{N}$  and Ti metal. On

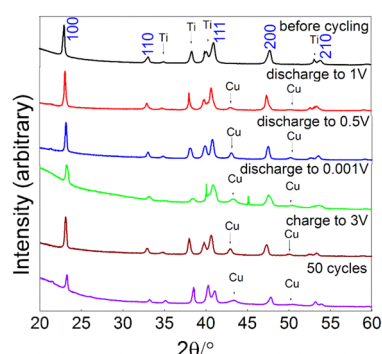


**Figure 5.** Ex situ XRD patterns of  $\text{Cu}_3\text{N}$  derived from copper pivalate cycled in sodium-ion batteries. Reflections from the titanium current collector are labeled and the reflections due to  $\text{Cu}_3\text{N}$  are marked by Miller indices in the top pattern, and reflections due to copper metal produced by reduction of  $\text{Cu}_3\text{N}$  are labeled in subsequent patterns.<sup>49</sup>

reducing  $\text{Cu}_3\text{N}$  to a series of different potentials, reflections due to metallic copper were observed to grow, but these did not diminish on oxidizing back to 3 V. After 50 cycles,  $\text{Cu}_3\text{N}$  and Cu are still present in roughly the same proportions, although the reflections are broadened somewhat, suggesting some loss of crystallinity. In a previous study, Pereira et al. cycled  $\text{Cu}_3\text{N}$  vs Li and found that, with relatively large crystallites ( $\sim 100$  nm), complete conversion to Cu metal was observed.<sup>42</sup> This may have been aided by lithium intercalation into the  $\text{Cu}_3\text{N}$  structure, as observed through an expansion of the unit cell from  $a = 3.81$  to  $3.84$  Å in the initial stages of reduction.<sup>42</sup> Interestingly, they also did not achieve full conversion back to  $\text{Cu}_3\text{N}$ . The  $\text{Cu}_3\text{N}$  lattice parameter was measured as  $3.8309(4)$  Å at 1 V,  $3.8226(5)$  Å at 0.5 V,  $3.8174(7)$  Å at 0.001 V,  $3.8394(4)$  Å after recharging to 3 V, and  $3.7928(5)$  Å at 3 V after 50 cycles. These variations likely reflect the scatter in the refined values due to the broad reflections and small amount of material measured, and do not provide compelling evidence for intercalation. It is likely that  $\text{Cu}_3\text{N}$  is mainly storing charge by a conversion mechanism, but that only a small proportion of the material is being converted, and that neither the reduction nor the oxidation process is fully reversible even in that surface region of the particles. If the surface region is responsible for much of the activity, it follows that smaller still particle sizes will provide larger capacities.

**3.2.  $\text{Cu}_3\text{N}$  Electrochemistry in Li Half Cells.** Since the  $\text{Cu}_3\text{N}$  material studied here had a smaller crystallite size than

that previously reported by Pereira et al.,<sup>42</sup> we also examined its lithium electrochemistry in Li half cells using a 1 M  $\text{LiPF}_6$  in 1:1 EC:DMC electrolyte. As with sodium, a large irreversible reduction was observed in the first cycle (Figure 6) and this

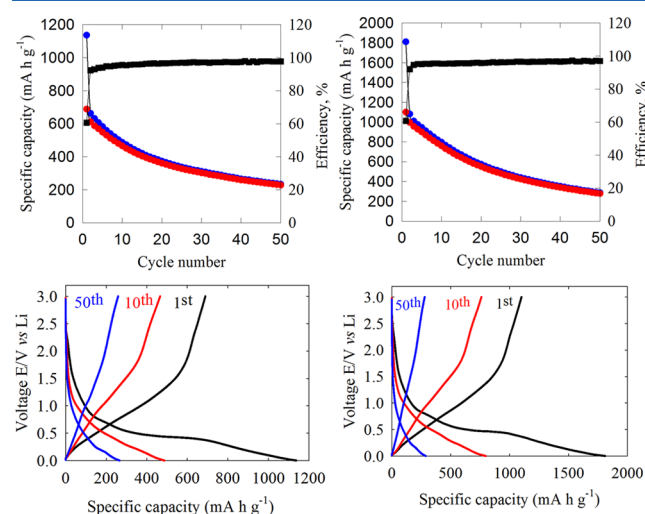


**Figure 6.** Voltage profile against specific cycles (bottom) and specific capacity versus cycle number profile (top) of  $\text{Cu}_3\text{N}$ -lithium half cells cycled between 1 mV and 3 V for cycles at 1C (392  $\text{mA h g}^{-1}$ , left), 0.5C (196  $\text{mA h g}^{-1}$ , right). In the specific capacity vs cycle number plots, blue circles show specific reduction capacity, red circles show specific oxidation capacity, and black squares depict Coulombic efficiency.

quickly settled into a stable cyclic pattern with only a gradual capacity loss. The galvanostatic plots obtained during cycling closely resemble those of Pereira et al. with a long plateau at  $\sim 0.5$  V in the first reduction attributed to lithium intercalation, followed by reduction, but the capacity changes with extended cycling are very different. We observed much higher specific capacities at the start of cycling (first cycle reduction 1135  $\text{mA h g}^{-1}$  at 1C or 1811  $\text{mA h g}^{-1}$  at 0.5C; first oxidation 663  $\text{mA h g}^{-1}$  at 1C or 1082  $\text{mA h g}^{-1}$  at 0.5C) and then a gradual reduction in capacity to the 50th cycle (233  $\text{mA h g}^{-1}$  at 1C or 287  $\text{mA h g}^{-1}$  at 0.5C). At these rates, Pereira et al. observed modest capacities in the early stages of cycling ( $\sim 640$   $\text{mA h g}^{-1}$  in the first reduction, dropping to  $\sim 250$   $\text{mA h g}^{-1}$  after 20 cycles) but then a gradual increase to  $>300$   $\text{mA h g}^{-1}$  after 200 cycles. Their larger crystallites broke into smaller units as cycling progressed, whereas ours were small from the beginning.

**3.3.  $\text{CuO}$  Electrochemistry in Na Half Cells.** In an attempt to improve the electrode fabrication process by depositing from a water-based ink with carboxymethyl cellulose (CMC), the  $\text{Cu}_3\text{N}$  was inadvertently converted to  $\text{CuO}$ . This material exhibited good electrochemical behavior vs sodium with a 196  $\text{mA h g}^{-1}$  cycling rate (equivalent to 0.29C based on complete reduction of  $\text{CuO}$  to copper metal and  $\text{Na}_2\text{O}$ ). A charge of 795  $\text{mA h g}^{-1}$  was passed in the first reduction, and 419  $\text{mA h g}^{-1}$  of this was recovered in the first oxidation. As with the other materials, the efficiency approached 100% after the first 2–3 cycles (Figure 7), but the capacity gradually dropped, with 138  $\text{mA h g}^{-1}$  passed in the 30th reduction cycle. Klein et al. previously examined the performance of  $\text{CuO}$  in half cells vs sodium and observed a similar first reduction potential curve to that shown in Figure 7, though with a shorter plateau at 1.5–1.0 V and a lower first reduction capacity of

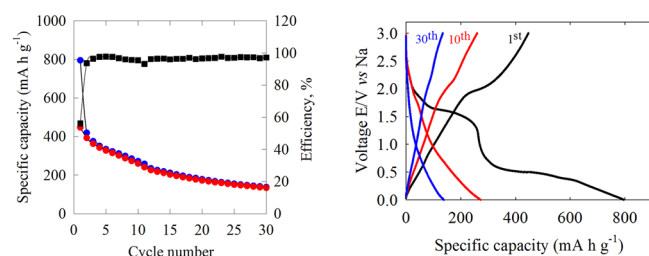


**Figure 7.** Voltage profile against specific cycles (left) and specific capacity for several different cycles (right) of CuO hydrolyzed from Cu<sub>3</sub>N-sodium half cells cycled between 1 mV and 3 V for cycles at 196 mA g<sup>-1</sup>. In the specific capacity vs cycle number plots, closed circles show specific reduction capacity, open circles show specific oxidation capacity, and squares depict Coulombic efficiency.

~600 mA h g<sup>-1</sup>.<sup>34</sup> The plateau at ~0.5 V tailing down to 0 V is of similar shape and length. They only presented 5 reduction/oxidation cycles, but their capacities at this point were similar to ours.

A previous report shows that reduction of CuO in a lithium electrolyte results in complete conversion to Cu<sub>2</sub>O, with partial conversion back to CuO observed on reoxidation.<sup>34</sup> In our study, reduction vs sodium to a potential of 0.8 V, i.e., just beyond the first plateau in the reduction profile shown in Figure 7, resulted in peaks due to Cu<sub>2</sub>O and Cu metal (Figure 8), and reduction to 1 mV resulted in complete reduction to Cu

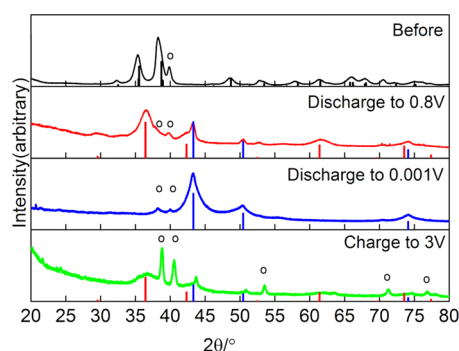


**Figure 8.** Ex situ XRD of CuO derived from oxidation of copper nitride discharged at 0.1C to different voltages in the first cycle. The black vertical lines show the standard positions of CuO reflections, the red of Cu<sub>2</sub>O, and the blue of Cu metal.<sup>49</sup> Open circles show the positions of reflections from the Ti substrate. Lattice parameters: CuO (before reduction)  $a = 4.6831(18)$  Å,  $b = 3.4132(14)$  Å,  $c = 5.1102(18)$  Å; Cu<sub>2</sub>O (0.8 V)  $a = 4.253(3)$  Å; Cu (0.001 V)  $a = 3.636(3)$  Å.

metal. The changes in the active material after the first plateau show that this plateau is not due solely to SEI formation. The Cu peaks are also significantly broadened relative to the CuO starting material, indicating a reduction in crystallite size. Oxidation back to 3 V results in formation of Cu<sub>2</sub>O and some Cu metal still remains, in contrast to the phase behavior previously observed vs lithium.<sup>34</sup>

#### 4. CONCLUSIONS

Cu<sub>3</sub>N derived from the ammonolysis of copper(II) pivalate exhibits a competitive negative electrode behavior in sodium cells. After an initial conditioning period, the capacity is reversible and is stable over 50 cycles at rates between 1C and 0.1C, with 89 mA h g<sup>-1</sup> observed on the 50th cycle at 0.1C. Ex

situ XRD shows the formation of metallic copper in the first cycle, but the Cu<sub>3</sub>N is retained throughout. Hence, the reactions appear to take place mainly at the surface of the particles. This Cu<sub>3</sub>N provided similar behavior in lithium cells to that reported previously, with 287 mA h g<sup>-1</sup> on the 50th cycle at 0.5C. Exposure to water resulted in hydrolysis and the formation of CuO, which gave larger initial capacities in sodium cells but was less stable during cycling, with 138 mA h g<sup>-1</sup> on the 30th cycle at 0.29C. In these cells, CuO was reduced to Cu<sub>2</sub>O and then to Cu metal, with partial reoxidation to Cu<sub>2</sub>O and copper metal on oxidizing back to 3 V.

#### ■ ASSOCIATED CONTENT

##### Supporting Information

Rietveld fits to the XRD patterns and TEM images of Cu<sub>3</sub>N produced from copper(II) pivalate and copper(II) fluoride, and electrochemical data collected to understand the effect of the acetylene black conductivity additive. This material is available free of charge via the Internet at <http://pubs.acs.org>.

#### ■ AUTHOR INFORMATION

##### Corresponding Author

\*E-mail: A.L.Hector@soton.ac.uk. Phone: +44 23 8059 4125 (A.L.H.).

##### Notes

The authors declare no competing financial interest.

#### ■ ACKNOWLEDGMENTS

The authors thank EPSRC for funding the Smartlab diffractometer under EP/K00509X/1 and EP/K009877/1, and acknowledge the use of the EPSRC-funded National Chemical Database Service hosted by the Royal Society of Chemistry.

#### ■ REFERENCES

- (1) Kim, S.-W.; Seo, D.-H.; Ma, X.; Ceder, G.; Kang, K. Electrode materials for rechargeable sodium-ion batteries: Potential alternatives to current lithium-ion batteries. *Adv. Energy Mater.* **2012**, *2*, 710–721.
- (2) Palomares, V.; Serras, P.; Villaluenga, I.; Hueso, K. B.; Carretero-Gonzalez, J.; Rojo, T. Na-ion batteries, recent advances and present challenges to become low cost energy storage systems. *Energy Environ. Sci.* **2012**, *5*, 5884–5901.
- (3) Slater, M. D.; Kim, D.; Lee, E.; Johnson, C. S. Sodium-ion batteries. *Adv. Funct. Mater.* **2013**, *23*, 947–958.
- (4) Ellis, B. L.; Nazar, L. F. Sodium and sodium-ion energy storage batteries. *Curr. Opin. Solid State Mater. Sci.* **2012**, *16*, 168–177.
- (5) Caballero, A.; Hernan, L.; Morales, J.; Sanchez, L.; Santos Pena, J.; Aranda, M. A. G. Synthesis and characterization of high-temperature hexagonal P2-Na<sub>0.6</sub>MnO<sub>2</sub> and its electrochemical behaviour as cathode in sodium cells. *J. Mater. Chem.* **2002**, *12*, 1142–1147.
- (6) Cao, Y.; Xiao, L.; Wang, W.; Choi, D.; Nie, Z.; Yu, J.; Saraf, L. V.; Yang, Z.; Liu, J. Reversible sodium ion insertion in single crystalline manganese oxide nanowires with long cycle life. *Adv. Mater.* **2011**, *23*, 3155–3160.
- (7) Liu, H.; Zhou, H.; Chen, L.; Tang, Z.; Yang, W. Electrochemical insertion/deinsertion of sodium on NaV<sub>6</sub>O<sub>15</sub> nanorods as cathode material of rechargeable sodium-based batteries. *J. Power Sources* **2011**, *196*, 814–819.
- (8) Tepavcevic, S.; Xiong, H.; Stamenkovic, V. R.; Zuo, X.; Balasubramanian, M.; Prakapenka, V. B.; Johnson, C. S.; Rajh, T. Nanostructured bilayered vanadium oxide electrodes for rechargeable sodium-ion batteries. *ACS Nano* **2012**, *6*, 530–538.
- (9) Mendiboure, A.; Delmas, C.; Hagenmuller, P. Electrochemical intercalation and deintercalation of Na<sub>x</sub>MnO<sub>2</sub> bronzes. *J. Solid State Chem.* **1985**, *57*, 323–331.

- (10) Bhide, A.; Hariharan, K. Physicochemical properties of  $\text{Na}_x\text{CoO}_2$  as a cathode for solid state sodium battery. *Solid State Ionics* **2011**, *192*, 360–363.
- (11) Lu, Y.; Wang, L.; Cheng, J.; Goodenough, J. B. Prussian blue: A new framework of electrode materials for sodium batteries. *Chem. Commun.* **2012**, *48*, 6544–6546.
- (12) Moreau, P.; Guyomard, D.; Gaubicher, J.; Boucher, F. Structure and stability of sodium intercalated phases in olivine  $\text{FePO}_4$ . *Chem. Mater.* **2010**, *22*, 4126–4128.
- (13) Jian, Z.; Zhao, L.; Pan, H.; Hu, Y.-S.; Li, H.; Chen, W.; Chen, L. Carbon coated  $\text{Na}_3\text{V}_2(\text{PO}_4)_3$  as novel electrode material for sodium ion batteries. *Electrochem. Commun.* **2012**, *14*, 86–89.
- (14) Xu, M.; Wang, L.; Zhao, X.; Song, J.; Xie, H.; Lu, Y.; Goodenough, J. B.  $\text{Na}_3\text{V}_2\text{O}_2(\text{PO}_4)_2\text{F}$ /graphene sandwich structure for high-performance cathode of a sodium-ion battery. *Phys. Chem. Chem. Phys.* **2013**, *15*, 13032–13037.
- (15) Ge, P.; Foulletier, M. Electrochemical intercalation of sodium in graphite. *Solid State Ionics* **1988**, *28*, 1172–1175.
- (16) Alcántara, R.; Jiménez-Mateos, J. M.; Lavela, P.; Tirado, J. L. Carbon black: A promising electrode material for sodium-ion batteries. *Electrochem. Commun.* **2001**, *3*, 639–642.
- (17) Komaba, S.; Murata, W.; Ishikawa, T.; Yabuuchi, N.; Ozeki, T.; Nakayama, T.; Ogata, A.; Gotoh, K.; Fujiwara, K. Electrochemical Na insertion and solid electrolyte interphase for hard-carbon electrodes and application to Na-ion batteries. *Adv. Funct. Mater.* **2011**, *21*, 3859–3867.
- (18) Wenzel, S.; Hara, T.; Janek, J.; Adelhelm, P. Room-temperature sodium-ion batteries: Improving the rate capability of carbon anode materials by templating strategies. *Energy Environ. Sci.* **2011**, *4*, 3342–3345.
- (19) Luo, W.; Schardt, J.; Bommier, C.; Wang, B.; Razink, J.; Simonsen, J.; Ji, X. Carbon nanofibers derived from cellulose nanofibers as a long-life anode material for rechargeable sodium-ion batteries. *J. Mater. Chem. A* **2013**, *1*, 10662–10666.
- (20) Cao, Y.; Xiao, L.; Sushko, M. L.; Wang, W.; Schwenzer, B.; Xiao, J.; Nie, Z.; Saraf, L. V.; Yang, Z.; Liu, J. Sodium ion insertion in hollow carbon nanowires for battery applications. *Nano Lett.* **2012**, *12*, 3783–3787.
- (21) Wu, L.; Pei, F.; Mao, R.; Wu, F.; Wu, Y.; Qian, J.; Cao, Y.; Ai, X.; Yang, H. SiC-Sb-C nanocomposites as high-capacity and cycling-stable anode for sodium-ion batteries. *Electrochim. Acta* **2013**, *87*, 41–45.
- (22) Qian, J.; Chen, Y.; Wu, L.; Cao, Y.; Ai, X.; Yang, H. High capacity Na-storage and superior cyclability of nanocomposite Sb/C anode for Na-ion batteries. *Chem. Commun.* **2012**, *48*, 7070–7072.
- (23) Xiao, L.; Cao, Y.; Xiao, J.; Wang, W.; Kovarik, L.; Nie, Z.; Liu, J. High capacity, reversible alloying reactions in SnSb/C nanocomposites for Na-ion battery applications. *Chem. Commun.* **2012**, *48*, 3321–3323.
- (24) Datta, M. K.; Epur, R.; Saha, P.; Kadakia, K.; Park, S. K.; Kumta, P. N. Tin and graphite based nanocomposites: Potential anode for sodium ion batteries. *J. Power Sources* **2013**, *225*, 316–322.
- (25) Zhu, H.; Jia, Z.; Chen, Y.; Weadock, N.; Wan, J.; Vaaland, O.; Han, X.; Li, T.; Hu, L. Tin anode for sodium-ion batteries using natural wood fiber as a mechanical buffer and electrolyte reservoir. *Nano Lett.* **2013**, *13*, 3093–3100.
- (26) Baggetto, L.; Keum, J. K.; Browning, J. F.; Veith, G. M. Germanium as negative electrode material for sodium-ion batteries. *Electrochem. Commun.* **2013**, *34*, 41–44.
- (27) Qian, J.; Wu, X.; Cao, Y.; Ai, X.; Yang, H. High capacity and rate capability of amorphous phosphorus for sodium ion batteries. *Angew. Chem., Int. Ed.* **2013**, *52*, 4633–4636.
- (28) Xiong, H.; Slater, M. D.; Balasubramanian, M.; Johnson, C. S.; Rajh, T. Amorphous  $\text{TiO}_2$  nanotube anode for rechargeable sodium ion batteries. *J. Phys. Chem. Lett.* **2011**, *2*, 2560–2565.
- (29) Alcántara, R.; Jaraba, M.; Lavela, P.; Tirado, J. L.  $\text{NiCo}_2\text{O}_4$  spinel: First report on a transition metal oxide for the negative electrode of sodium-ion batteries. *Chem. Mater.* **2002**, *14*, 2847–2848.
- (30) Koo, B.; Chattopadhyay, S.; Shibata, T.; Prakapenka, V. B.; Johnson, C. S.; Rajh, T.; Shevchenko, E. V. Intercalation of sodium ions into hollow iron oxide nanoparticles. *Chem. Mater.* **2013**, *25*, 245–252.
- (31) Bi, Z.; Paranthaman, M. P.; Menchhofer, P. A.; Dehoff, R. R.; Bridges, C. A.; Chi, M.; Guo, B.; Sun, X.-G.; Dai, S. Self-organized amorphous  $\text{TiO}_2$  nanotube arrays on porous Ti foam for rechargeable lithium and sodium ion batteries. *J. Power Sources* **2013**, *222*, 461–466.
- (32) Klein, F.; Jache, B.; Bhide, A.; Adelhelm, P. Conversion reactions for sodium-ion batteries. *Phys. Chem. Chem. Phys.* **2013**, *15*, 15876–15887.
- (33) Wang, Y.; Yu, X.; Xu, S.; Bai, J.; Xiao, R.; Hu, Y.-S.; Li, H.; Yang, X.-Q.; Chen, L.; Huang, X. A zero-strain layered metal oxide as the negative electrode for long-life sodium-ion batteries. *Nat. Commun.* **2013**, *4*, 2365.
- (34) Park, Y.; Shin, D.-S.; Woo, S. H.; Choi, N. S.; Shin, K. H.; Oh, S. M.; Lee, K. T.; Hong, S. Y. Sodium terephthalate as an organic anode material for sodium ion batteries. *Adv. Mater.* **2012**, *24*, 3562–3567.
- (35) Zhao, L.; Zhao, J.; Hu, Y.-S.; Li, H.; Zhou, Z.; Armand, M.; Chen, L. Disodium terephthalate ( $\text{Na}_2\text{C}_8\text{H}_4\text{O}_4$ ) as high performance anode material for low-cost room-temperature sodium-ion battery. *Adv. Energy Mater.* **2012**, *2*, 962–965.
- (36) Deng, W.; Liang, X.; Wu, X.; Qian, J.; Cao, Y.; Ai, X.; Feng, J.; Yang, H. A low cost, all-organic Na-ion battery based on polymeric cathode and anode. *Sci. Rep.* **2013**, *3*, 2671.
- (37) Li, X.; Hasan, M. M.; Hector, A. L.; Owen, J. R. Performance of nanocrystalline  $\text{Ni}_3\text{N}$  as a negative electrode for sodium-ion batteries. *J. Mater. Chem. A* **2013**, *1*, 6441–6445.
- (38) Juza, R.; Hahn, H. Über die kristallstrukturen von  $\text{Cu}_3\text{N}$ , GaN und InN metallamide und metallnitride. *Z. Anorg. Allg. Chem.* **1938**, *239*, 282–287.
- (39) Hahn, U.; Weber, W. Electronic structure and chemical-bonding mechanism of  $\text{Cu}_3\text{N}$ ,  $\text{Cu}_3\text{NPd}$ , and related Cu(I) compounds. *Phys. Rev. B* **1996**, *53*, 12684–12693.
- (40) Zachwieja, U.; Jacobs, H. Copper palladium nitrides,  $\text{Cu}_3\text{Pd}_x\text{N}$  where  $x = 0.020$  and  $0.989$ , perovskites with binding  $3d^{10}-4d^{10}$  interaction. *J. Less-Common. Met.* **1991**, *170*, 185–190.
- (41) Paniconi, G.; Stoeva, Z.; Doberstein, H.; Smith, R. I.; Gallagher, B. L.; Gregory, D. H. Structural chemistry of  $\text{Cu}_3\text{N}$  powders obtained by ammonolysis reactions. *Solid State Sci.* **2007**, *9*, 907–913.
- (42) Pereira, N.; Dupont, L.; Tarascon, J. M.; Klein, L. C.; Amatucci, G. G. Electrochemistry of  $\text{Cu}_3\text{N}$  with lithium - A complex system with parallel processes. *J. Electrochem. Soc.* **2003**, *150*, A1273–A1280.
- (43) Larson, A. C.; Von Dreele, R. B. *Generalized Structure Analysis System (GSAS)*; Los Alamos National Laboratory Report LAUR; The Regents of the University of California: Berkeley, CA, 2004; pp 86–748.
- (44) Toby, B. H. EXPGUI, a graphical user interface for GSAS. *J. Appl. Crystallogr.* **2001**, *34*, 210–213.
- (45) Brunauer, S.; Emmett, P. H.; Teller, E. Adsorption of gases in multimolecular layers. *J. Am. Chem. Soc.* **1938**, *60*, 309–319.
- (46) Choi, J.; Gillan, E. G. Solvothermal synthesis of nanocrystalline copper nitride from an energetically unstable copper azide precursor. *Inorg. Chem.* **2005**, *44*, 7385–7393.
- (47) Wu, H.; Chen, W. Copper nitride nanocubes: size-controlled synthesis and application as cathode catalyst in alkaline fuel cells. *J. Am. Chem. Soc.* **2011**, *133*, 15236–15239.
- (48) Paniconi, G. Ph.D. Thesis, University of Nottingham, Nottingham, U.K., 2012.
- (49) Inorganic Crystal Structure Database (ICSD, Fiz Karlsruhe) accessed via the National Chemical Database Service hosted by the Royal Society of Chemistry. Record numbers used were 64699 ( $\text{Cu}$ ), 40056 ( $\text{Cu}_3\text{N}$ ), 43416 ( $\text{Ti}$ ), 92368 ( $\text{CuO}$ ), and 52043 ( $\text{Cu}_2\text{O}$ ).